Nano Research 2016, 9(2): 507–516
DOI 10.1007/s12274-015-0932-6
Research Article
ISSN 1998-0124
CN 11-5974/O4

Enhanced rectification, transport property and photocurrent generation of multilayer $ReSe_2/MoS_2$ p–n heterojunctions

Xiaoting Wang[1], Le Huang[1], Yuting Peng[2], Nengjie Huo[1], Kedi Wu[3], Congxin Xia[2], Zhongming Wei[1] (✉), Sefaattin Tongay[3] (✉), and Jingbo Li[1] (✉)

[1] *State Key Laboratory of Superlattices and Microstructures, Institute of semiconductors, Chinese Academy of Sciences, P.O. Box 912, Beijing 100083, China*
[2] *Physics and Electronic Engineering College, Henan Normal University, Xinxiang 453007, China*
[3] *School for Engineering of Matter, Transport and Energy, Arizona State University, Tempe, Arizona 85287, USA*

Received: 28 August 2015
Revised: 25 October 2015
Accepted: 29 October 2015

KEYWORDS
$ReSe_2/MoS_2$,
van der Waals heterojunction,
rectification,
optoelectronic properties

ABSTRACT

Van der Waals (vdW) heterojunctions are equipped to avert dangling bonds due to weak, inter-layer vdW force, and ensure strong in-plane covalent bonding for two-dimensional layered structures. We fabricated four heterojunctions devices of different layers based on p-type distorted 1T-MX_2 $ReSe_2$ and n-type hexagonal MoS_2 nanoflakes, and measured their electronic and optoelectronic properties. The device showed a high rectification coefficient of 500 for the diode, a high ON/OFF ratio and higher electron mobility for the field-effect transistor (FET) compared with the individual components, and a high current responsivity (R_λ) and external quantum efficiency (EQE) of 6.75 A/W and 1,266%, respectively, for the photodetector.

1 Introduction

As one of the most important systems among industrial semiconductors, p–n heterojunctions have attracted considerable attention because of their promising applications in electronic and optoelectronic devices [1–3]. Traditional heterojunctions are primarily centered on IV, III-V, or II-VI semiconductors connected by covalent bonds between atoms at the interface [4]. The selection of covalent materials as elementary units could lead to lattice mismatch owing to the differences in lattice constants or the crystallographic orientation at interface. Lattice mismatch is prone to induce formation of dangling bonds and further misfit dislocations. Dangling bonds at the interface can work as the recombination centers or carrier traps to absorb

Address correspondence to Zhongming Wei, zmwei@semi.ac.cn; Sefaattin Tongay, sefaattin.tongay@asu.edu; Jingbo Li, jbli@semi.ac.cn

free charge carriers. This could directly result in the low quantum efficiency and negate the functionalities of devices.

Recently, two-dimensional (2D) materials have been widely studied as potential active channels in nanoelectronic devices [5–11]. Further, the precise "dry transfer" method for creating p–n van der Waals (vdW) heterostructures has pioneered a pathway for the new field of 2D nanomaterial heterostructures. These heterostructures possess novel functionalities in comparison with their component members, and show tremendous potentials in electronics and optoelectronics such as field-effect transistors (FETs), photovoltaic cells, rectifiers, and light-emitting diodes [12–15]. In contrast with the covalent semiconductors, vdW layered materials are in-plane covalently bonded 2D materials with the adjacent layers linked by weak vdW forces [16–20]. By complex stacking one vdW material on top of the other more, various heterostructures can be created with novel highly tailored electronic or optoelectronic qualities superior to isolated materials [21]. The key advantage of the vdW/vdW heterostructures is the absence of dangling bonds on the surface of vdW layered materials, which makes it possible to obtain superior heterointerfaces without restrictions of lattice parameters or direction lattice planes.

In most previous reports, vdW/vdW heterostructures are composed of graphene, few-layer hBN, MoS_2, WS_2 and WSe_2, and $MoSe_2$ [1, 5, 16, 22, 23], with a simple planar hexagonal lattice structure [24]. Herein, we report on vertical heterojunctions made from multilayer exfoliated n-type MoS_2 and p-type $ReSe_2$ nanoflakes. $ReSe_2$ belongs to the indirect semiconductor and exists in a distorted 1T in-plane structure of triclinic symmetry, with a clustering of zigzag Re chain along the *b*-axis. $ReSe_2$ is an optically biaxial material that possesses extremely anisotropic electrical and optical features for linearly polarized light. Recently, few-layer $ReSe_2$-based field-effect transistors have been fabricated and demonstrated to have a p-type property and a mobility of 0.1 $cm^2/(V{\cdot}s)$. One component has a normal hexagonal structure (MoS_2) and the other has a distorted $CdCl_2$ structure ($ReSe_2$), which extends the family of vdW heterojunctions [25]. Despite the structurally vast spread of the constituent parts, the absence of dangling bonds in vdW heterostructures enables such system to present significant rectifying behavior with a high forward to reverse current ratio. FETs based on this heterojunction showed much higher electron mobility than the individual components, with a high on/off ratio. In addition, this heterojunction also worked as efficient photodetector for red laser with very high current responsivity (R_λ) and external quantum efficiency (EQE).

Thus, the asymmetric structured (opto)electronics based on such heterojunctions are experimentally confirmed to possess preferable functionalities to single component $ReSe_2$ or MoS_2 devices, including obvious rectification, elevated electron mobility and on–off current ratio, and efficient photocurrent generation. Considering first-principles methods can provide an exact theoretical account for vdW–vdW heterojunctions [26], the Vienna *ab initio* simulation package (VASP) was employed to calculate the band alignment of $ReSe_2$ and MoS_2 materials and give a standard p–n junction arrangement for the $ReSe_2/MoS_2$ heterojunctions, which also agree well with our experimental results.

2 Results and discussion

Before the fabrication of different kinds of (opto)electronic devices, both multilayer $ReSe_2$ and MoS_2 flakes were acquired by exfoliation from "parent" bulk material, and then, the $ReSe_2$ flakes were transferred onto the top of the MoS_2 flakes. Then, metal electrode contacts were processed on the Si/SiO_2 substrates by using standard photolithography technique and e-beam evaporation.

Figure 1(a) shows a typical optical microscope image of the device based on p–n $ReSe_2/MoS_2$ heterojunction. Figure 1(b) describes the cross-sectional drawing of the heterojunction together with thin Cr/Au film (5/80 nm) electrodes, deposited on top of Si/SiO_2 substrate. These two electrodes served as the source and drain. The Si substrate was used as a back gate.

The atomic force microscope (AFM) image (Fig. 1(c)) of the device confirmed that the thicknesses of $ReSe_2$ and MoS_2 flakes were about 60 and 7 nm, respectively, based on the cross-sectional height profile along the line shown above. A combination of AFM, energy dispersive X-ray spectroscopy (EDX) described in the

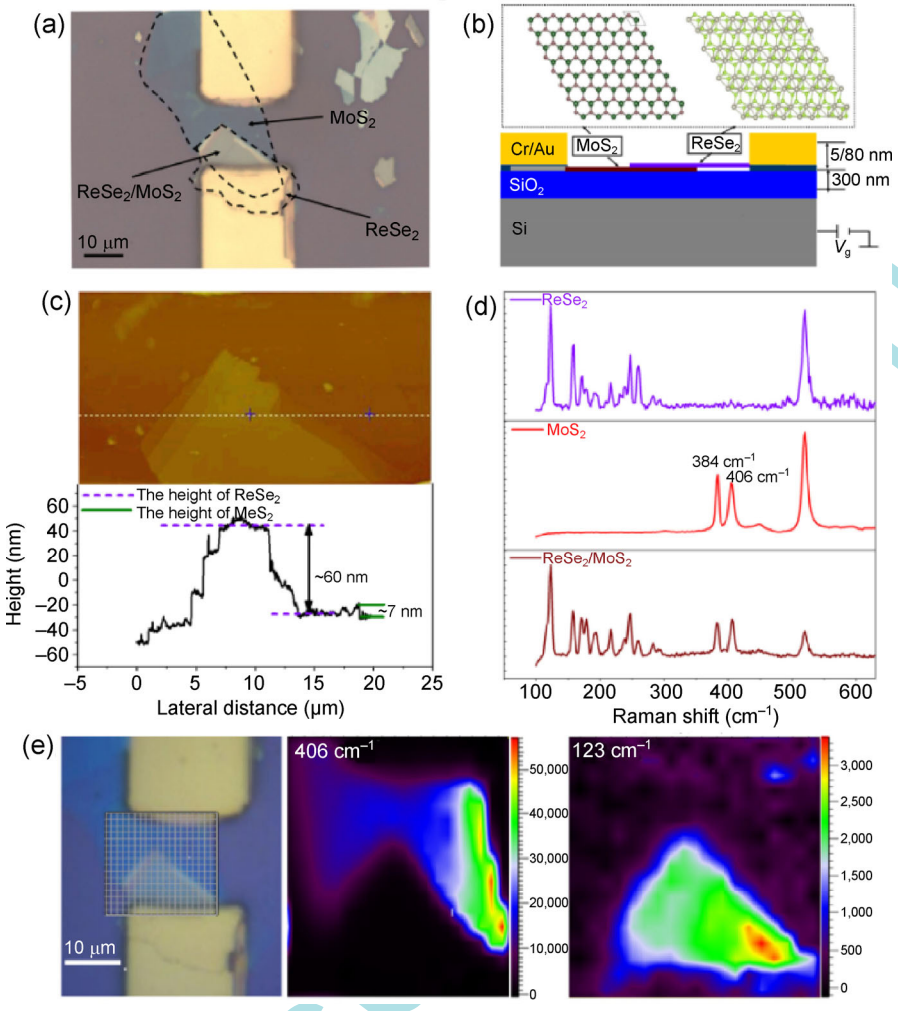

Figure 1 Characterization of $ReSe_2/MoS_2$ heterojunction and device. (a) Optical microscope image of the device based on the p-n $ReSe_2/MoS_2$ heterojunction; (b) schematic of the FET device. Top: in-plane atomic arrangement structure of MoS_2 and $ReSe_2$, with dark green, red, gray, and light green microspheres representing Mo, S, Re, and Se, respectively; (c) top: AFM image of the device channel. Bottom: cross-sectional plot along the red line on the top picture; (d) the Raman scattering spectra for the few layer $ReSe_2$ and MoS_2 nanoflakes, and as-transferred $ReSe_2/MoS_2$ heterostructures; (e) the Raman mapping at the Raman mode of 123 cm^{-1} ($ReSe_2$) and 406 cm^{-1} (MoS_2). It is noteworthy that the peak intensity of MoS_2 without the $ReSe_2$ as coverage is much stronger than that of MoS_2 beneath the $ReSe_2$, such that no signal appears at 406 cm^{-1} at the $ReSe_2/MoS_2$ heterostructure region.

Electronic Supplementary Material (ESM), and Raman spectroscopy was utilized for confirming the thickness and features of our heterostructure. Figure 1(d) clearly exhibits Raman spectra obtained at three different positions on the sample (60 nm $ReSe_2$ nanoflake, purple line; 7 nm MoS_2 nanoflake, red line; as-transferred $ReSe_2/MoS_2$ heterostructures, brown line).

The Raman spectra of a single MoS_2 nanoflake revealed strong signals from both the in-plane E^1_{2g} (Γ) and the out-of-plane A_{1g} (Γ) optical phonon modes at the Brillouin zone center, whose wavenumbers are 384 and 406 cm^{-1}, respectively. Nevertheless, $ReSe_2$ is crystallized in a distorted layered $CdCl_2$-type octahedral structure (Fig. 1(b)) [27], distinguishing it from most hexagonal layered TMDCs. The asymmetric structure of the layered $ReSe_2$ directly leads to its intricate Raman spectrum with more than ten obvious Raman peaks closely arranged. In addition, as shown in Fig. 1(d), the Raman spectrum of the as-transferred heterostructure was just the superposition of two kinds of nanosheets above, meaning that the signal of one nanosheet is independent of the other. Thus, the Raman spectra proved the formation and structure of the $ReSe_2/MoS_2$ heterostructure.

After point-scanning Raman scattering spectrum for the $ReSe_2/MoS_2$ heterostructure, the heterojunction was also investigated through Raman mapping measurements. The wavenumbers of $ReSe_2$ range from 100 to 300 cm^{-1}, while those for MoS_2 are around 400 cm^{-1}. Considering this wide variation, Raman mapping at 406 cm^{-1} (MoS_2) and 123 cm^{-1} ($ReSe_2$) clearly displayed sharp signals from each of the two nanoflakes with a rainbow color bar (Fig. 1(e)). For example, at 406 cm^{-1} (MoS_2), the single MoS_2 nanoflake region is denoted by the ultramarine color, whereas there was nearly no signal in the $ReSe_2/MoS_2$ heterostructure region. It is noteworthy that the peak intensity of MoS_2 without coverage is much stronger than that of MoS_2 beneath the $ReSe_2$ (almost no signal at that location). Therefore, the Raman mapping can elucidate the stacking structure of such heterojunctions: MoS_2 nanoflakes at the bottom overlapped locally by $ReSe_2$ nanoflakes on the top [28].

We first tested the I_{ds}–V_{ds} characteristics at V_g = 0 of such p–n heterojunctions device to make sure ohmic contact diodes were achieved. Devices based on individual $ReSe_2$ and few MoS_2 layers were also fabricated and characterized for control experiments. The observed I_{ds}–V_{ds} plot (Figs. S2(a) and S2(b) in the ESM) presents a slight-curve trend but still demonstrates that the Cr/Au electrode almost makes Ohmic connections with the MoS_2 or $ReSe_2$ nanoflakes, which prevents the Schottky barrier at the contact end from affecting the electronic or optoelectronic measurements on the device [28]. Meanwhile, the diode based on p–n $ReSe_2/MoS_2$ heterostructures exhibited well-defined current rectification behavior, as shown in Fig. 2(a). With the coordinate value of the head and the tail, we can quantitatively calculate the forward-to-reverse bias current ratio (rectification coefficient) to be around 500. The phenomenon of obvious rectification is one of the strong evidences that confirmed the efficient formation of $ReSe_2/MoS_2$ heterostructures and an asymmetric diode.

The FET device based on this heterojunction exhibited obvious n-type transport characteristics and high performance, as shown in Figs. 2(b) and 2(c). We further evaluated other electrical characteristics from the transfer curves of p–n heterojunction device. The transfer curve presented in Fig. 2(b) exhibited an

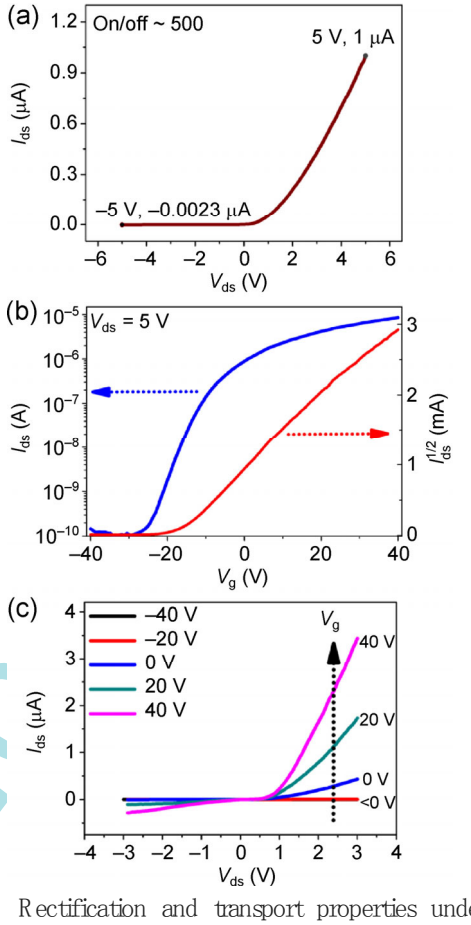

Figure 2 Rectification and transport properties under dark condition. (a) The I_{ds}–V_{ds} plot of p–n heterojunction rectifier; (b) the transfer and (c) output curves of p–n heterojunction transistor.

on–off current ratio as high as 6 × 10^4 of the vertical heterojunction, much higher than that of our isolated few-layer $ReSe_2$ or MoS_2 nanoflakes, (2 and 2 × 10^3 for $ReSe_2$ or MoS_2, respectively). The performance could be further improved by increasing the gate voltage V_g or drain–source bias V_{ds}. Therefore, although two kinds of nanoflakes were merely stacked up structurally, assuming that this could be referred to as a heterojunction, the property is indeed 30-fold higher than that of the individual components.

The field-effect mobility μ of the device can be expressed as $\mu = (L/WC_iV_{ds})\partial I_{ds}/\partial V_g$, where L is the channel length, W is the channel width, and C_i = 1.15 × 10^{-4} F/m^2 is the gate capacitance between the channel and the back gate per unit area ($C_i = \varepsilon\varepsilon_r/d$; ε = 8.85 × 10^{-12} F/m is vacuum permittivity; ε_r = 3.9 is relative permittivity of insulating barrier SiO_2; d = 300 nm is the thickness of the insulating barrier). In accordance with the data shown in Fig. 2(b), we can estimate that

the field-effect mobility is about 4 $cm^2/(V·s)$. Analogously, Figs. S3(a) and S3(b) indicate that the mobility of constituent members, $ReSe_2$ and MoS_2, was 0.145 (hole) and 0.226 (electron) $cm^2/(V·s)$, respectively. These results imply that the heterojunction can obviously enhance the electron mobility, and the transport of such a device was dominated by n-type MoS_2. MoS_2/$ReSe_2$ heterojunction devices were also machined and their electrical and optoelectronic properties were measured (Figs. S9(a)–S9(d) in the ESM). The results of the transfer curves as noted above are consistent with those of the output plots presented in Fig. 2(d). The few-layer heterojunction FETs exhibit similar properties with 60 nm-$ReSe_2$/7 nm-MoS_2. However, the rectification coefficient and the electron mobility were calculated to be 56 and 2.16 $cm^2/(V·s)$, respectively, which are lower than those of the thick sample.

The device was also tested under illumination to observe the photoresponsive property. A 633-nm red laser was used as the irradiation source, by vertically shining it onto the devices at room temperature in air. With the incidence of light upon the junction of the two dissimilar materials, the photovoltaic effect induces the generation of an electromotive force such as the open circuit voltage (V_{oc}). The normal rectifying I–V curve of the heterojunction under illumination (Fig. 3(a)) shows clear photovoltaic effect with an open-circuit voltage of around 0.1 V. Besides, Fig. 3(b) (black triangles) shows that a maximum output point of 6.53 pW was achieved at V_{ds} = 73.37 mV and I_{ds} = 89 pA.

The conversion efficiency was found to be 0.072% with a fill factor of 0.344. The low-level efficiency is largely triggered by the device structure [29, 30]. The long distance between the two electrodes is not conducive to charge separation, aggregation, and transmission, which increases the odds of interlayer recombination during diffusion. Even so, the results are still useful for further research in optimizing device structure. The transfer and output curves in Figs. 3(c) and 3(d) revealed that the device showed much better FET performance in the case of 8.15 mW/cm^2 red laser illumination. The electron mobility was calculated to be about 7 $cm^2/(V·s)$, which is almost twice the value in dark.

The photon-dependent electric curve can be well fitted by the power equation $I_{photo} = AP^{\alpha}$, where I_{photo}

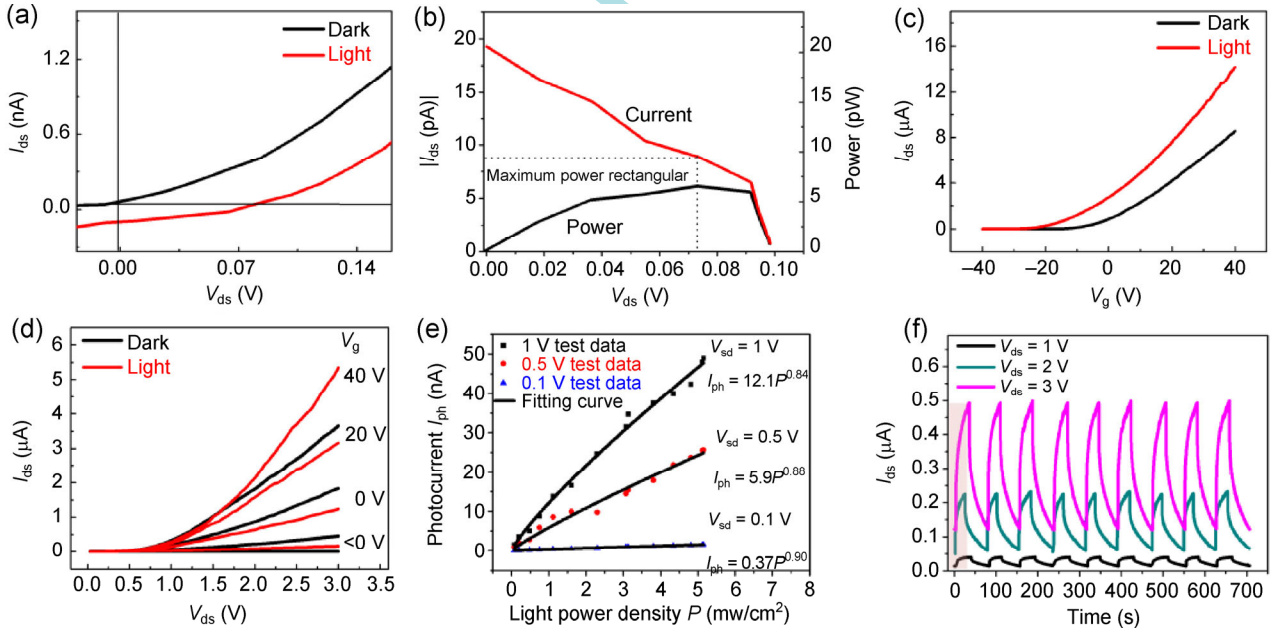

Figure 3 Photocurrent generation of $ReSe_2/MoS_2$ p–n heterojunctions. (a) I_{ds}–V_{ds} curves of our device in the dark and under illumination (wavelength: 633 nm; power density: 8.15 mW/cm^2); (b) the I–V curve and P–V curve of the device under 8.15 mW/cm^2 illumination. The rectangle denotes the coordinate of maximum output power; (c) transfer characteristics of the devices in the dark and under 8.15 mW/cm^2 light illumination; (d) output plots of the devices in the dark and under 8.15 mW/cm^2 light illumination; (e) photocurrent I_{ph} as a function of light power density ranging from 0.08 to 5.15 mW/cm^2 with V_{sd} of 0.1, 0.5, and 1 V, at V_g = 0 V; (f) drain–source current I_{ds} as a function of time with light switched on/off at V_{sd} from 1 to 3 V with the pink strip representing the light-on state.

($I_{photo} = I_{light} - I_{dark}$) is the net current increment under light, A is the proportionality constant, and α is the exponent depending on the photo response to the incident light intensity. Our experimental data of photocurrent exhibits an intensity dependence of 0.84, 0.88, or 0.90 on light power density at fixed biases of 1, 0.5, or 0.1 V, respectively, which confirms the effective generation of electron–hole pairs from absorbed photons. Moreover, note that the photocurrent visibly increases when the forward bias voltage is just increased by 0.5 V (Fig. 3(e)). Such drain-voltage-dependent photocurrent generation implies that a larger drain voltage can better contribute to the separation of electron–hole pairs and the acceleration to the electrode, or suppress the photogenerated charges from recombination [31–33].

Based on the data shown in Fig. 3(e), we can estimate R_λ and EQE, both critical parameters for photodetectors. R_λ refers to the photocurrent generated per unit power of the incident light on the per unit area of a photoelectric device, i.e., $R_\lambda = \Delta I_{ph}/P_\lambda S$. EQE is the number of electron–hole pairs excited by one incident photon, i.e., EQE = $hcR_\lambda/e\lambda$, where P is the incident light power, S is the effective illuminated area of the photodetector, h is Planck's constant, λ is the optical wavelength, and e is the electron charge. Herein, S = 141 μm^2, λ = 633 nm, and P = 5.15 mW/cm^2; then, ΔI_{ph} = 49 nA. Hence, the estimated value of R_λ and EQE can reach 6.75 A/W and 1,266% at an applied voltage of 1 V. According to the Figs. S5(c) and S5(d) in the ESM, the R_λ of $ReSe_2$ and MoS_2 can reach 2.22 and 4.03 A/W, respectively, at V_{ds} = 1 V.

Furthermore, the photocurrent increased with an increase in the drain-source voltage, until the light-induced charge generation reached the saturation point. We can reasonably infer that the R_λ and EQE will increase with increasing drain-source voltage. These performance parameters are better or paralleled to those of other existing photodetectors, as listed in Table 1 [34–36]. The above results illustrate that the selection of our heterojunction as a building block results in highly light-sensitive performance of the photodetector.

The photocurrent vs. time plots are measured under the same lamphouse with a constant light intensity of 8.15 mW/cm^2. It is apparent from Fig. 3(f) that each switching cycle of our device contains three sections, i.e. quick rise, stable state, and quick decay, which can be completed at roughly 80 s intervals. As we manually turn on or off the irradiation source, the output current I_{sd} can regularly switch between the high and low states rapidly. Moreover, consistent with the previous analysis, with the drain-source voltage varying from 1 to 3 V, the photocurrent indicates a distinctly absolute increment while the relative increment is almost equal; namely, the current on/off ratio increases by more than 4 times. Four representative wavelength sources (255 nm-ultraviolet, 405 nm-violet, 532 nm-green, and 633 nm-red) at the same power (2.48 mW/cm^2) are used to identify the variation with respect to wavelength of the heterojunction devices (see S8 in the ESM). It can be observed that the device is the most sensitive to red light, followed by green, violet, and ultraviolet light.

Table 1 Comparison of the performance parameters of photodetectors based on our device and previously reported 2D material

Photodetectors	R_λ (A/W)	EQE (%)	Ref.
Multilayer $ReSe_2/MoS_2$ heterostructures (V_{ds} = 1 V)	6.75	1,266	our work
Atomically sharp WSe_2/MoS_2 heterojunction (V_{ds}= 0 V)	—	1	[12]
Multilayer MoS_2–WS_2 heterojunctions (V_{ds}=1 V)	0.76	149	[34]
Three-layer MoS_2 (1.9 nm)	0.57	—	[35]
Four-layer GaSe (4.23 nm) (V_{ds}= 2 V)	2.8	1,367	[33]
Multilayer WS_2	5.7	1,118	[36]

Further, three $ReSe_2/MoS_2$ heterojunctions devices were fabricated and their electrical and photoelectrical properties evaluated, as shown in Table S1 (in the ESM). It is well-founded to believe that they possess good reproductivity. Much thinner heterojunctions (in which the thickness of both $ReSe_2$ and MoS_2 is less than 10 nm) were also investigated, but these show inferior properties than those of the thick samples (S11 in the ESM). Therefore, we mainly focus on 70 nm-$ReSe_2$/7 nm-MoS_2 heterojunctions in the text.

To realize the micro mechanism for high performance of the heterojunctions, the band alignments of few layer MoS_2 and $ReSe_2$ materials with vacuum level as reference were calculated using VASP [37]. The

generalized gradient approximation (GGA) of Perdew, Burke and Ernzerhof (PBE) functional is adopted for electron exchange and correlation [38]. The numerous high symmetry points of $ReSe_2$ (Fig. 4(a)) are attributed to its distorted structure and provide a clear illustration for complex Raman spectrum, whereas MoS_2 (Fig. 4(b)) as the hexagonal material merely exhibits two high symmetry points. These particular points in first Brillouin zones are labeled in Fig. S7 (in the ESM). Figure 4(c) shows the ideal band arrangement of p-type $ReSe_2$ and n-type MoS_2, presenting normal p–n type-II heterojunction characteristics, which were the radical cause for the good electrical characteristics. Further, the detailed principle interpretation is shown in Figs. 4(d)–4(i). Without bias (Fig. 4(d)), the hole and electrons are well restricted in $ReSe_2$ and MoS_2, respectively. At forward bias (above the threshold voltage) (Fig. 4(e)), the quasi-Fermi level of MoS_2 in the non-overlapped domain varies towards the valence band maximum, and that of $ReSe_2$ towards the conduction band minimum. The potential barrier decreases so that majority carrier can shift across the potential barrier from one region to the other. At negative bias (Fig. 4(f)), the quasi-Fermi level of MoS_2 in the non-overlapped domain varies towards the conduction band minimum, and that of $ReSe_2$ towards the valence band maximum. The potential barrier increase only allows minority carriers to diffuse across the barrier. The bottom-gate regulation can be interpreted qualitatively by the metal–insulator–semiconductor (MIS) model [39, 40]. When a negative gate voltage ($V_g < 0$) is applied to the device (Fig. 4(g)), the holes in p-type $ReSe_2$ are accumulated but the electrons in n-type MoS_2 are depleted. Hence, the MoS_2 region is regarded as the obstacle to the hole current, and the off-state current decreases. At $V_g > 0$ (Fig. 4(i)), electrons are accumulated in MoS_2. For p-type $ReSe_2$, the hole current is still large at $V_g = 40$ V, as shown in Fig. S3(a). Thus,

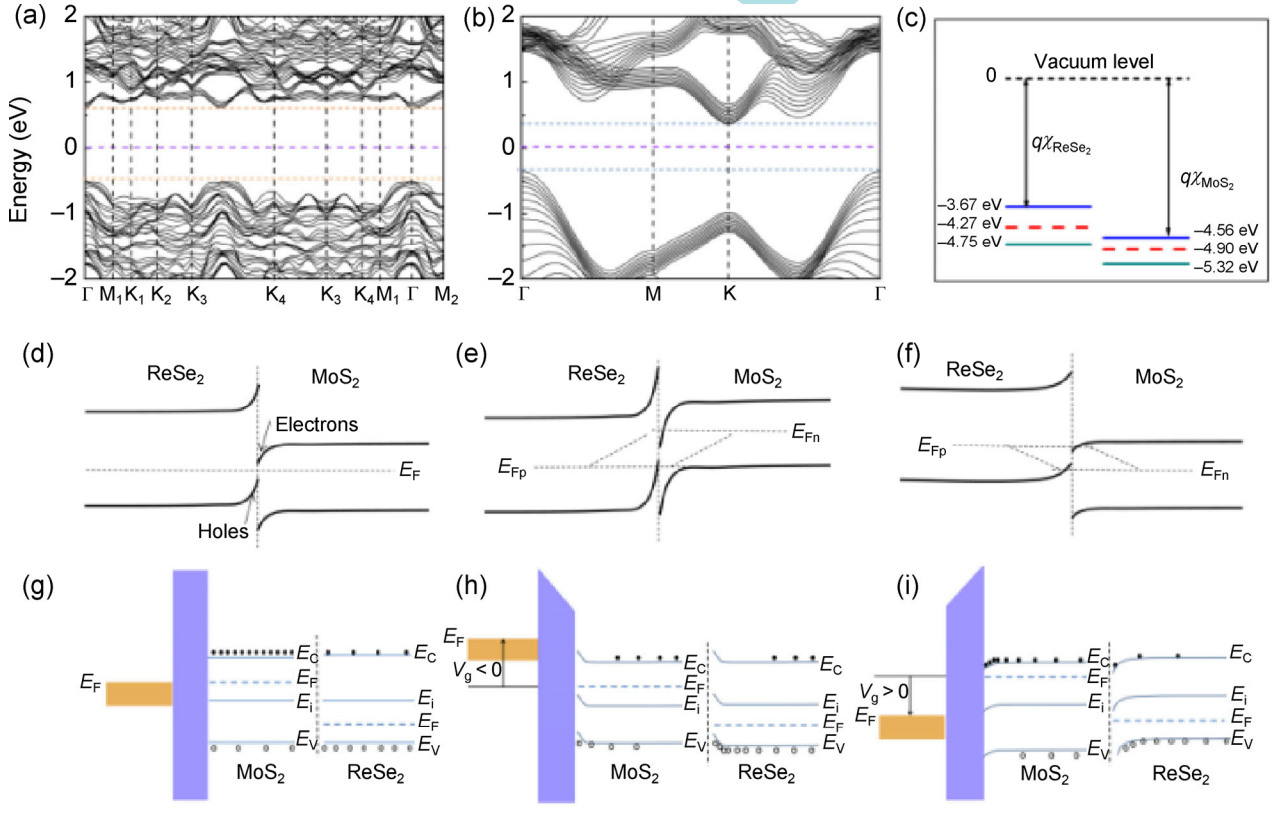

Figure 4 Theoretical calculations of $ReSe_2/MoS_2$ p–n heterojunctions. (a) Band structures of $ReSe_2$; (b) band structures of MoS_2. High symmetry points of brillouin zone are expressed by the vertical black dashed lines and the Fermi energy by the horizontal violet dotted line; (c) band arrangement for $ReSe_2$ and MoS_2 with the black horizon as the vacuum level. The symbol of $q\chi$ signals electron affinity; the ideal band diagram of $ReSe_2/MoS_2$ heterojunction under (d) $V_{ds} = 0$, (e) $V_{ds} > 0$ and (f) $V_{ds} < 0$; schematic energy band diagrams of $ReSe_2$ and MoS_2 at (g) $V_g = 0$, (h) $V_g < 0$ and (i) $V_g > 0$ using MIS model.

the on-state current increases owing to the open-state for both $ReSe_2$ and MoS_2.

As a type-II band alignment for our $ReSe_2/MoS_2$ heterojunctions, the conduction and valence band edge of $ReSe_2$ are higher than those of MoS_2. The potential difference gives rise to a built-in field at the junction interface. The electrical field drives the light-induced electrons and holes in the opposite directions, leading to a spatial separation of the electrons and holes on opposite sides of the heterojunction [41, 42]. Thus compared with the individual components, the $ReSe_2/MoS_2$ heterostructures contributes to the generation and momentary separation of light-induced electron–hole pairs extracted by the electrical fields and enhances charge separation efficiency for improved photocurrent generation [43]. Briefly, the VASP displays a standard p–n junction arrangement for the $ReSe_2/MoS_2$ heterojunctions, which are consistent with our experimental results.

3 Conclusions

In conclusion, we have created p–n $ReSe_2/MoS_2$ van der Waals heterostructures by the mechanical transfer technique and utilized it in several kinds of (opto)electronics including diodes, FETs, and red light photodetectors. The *I*–*V* plot, photoresponsive property, and Raman spectrum measurement demonstrate that such devices exhibit good diode characteristics with unilateral conductivity, and a p–n junction is efficiently formed. The diode based on such heterojunctions showed a high rectification coefficient of 500, with the absence of rectifying property in the individual components. The transport measurements exhibited high on/off current ratio of 6×10^4 and electron mobility of about 4 $cm^2/(V \cdot s)$, which are much higher than those of the individual parts ($ReSe_2$ or MoS_2). In addition, the heterojunction also showed obvious photoresponse to 633-nm red light, with an almost doubled electron mobility, drain-source current enhanced by 3 times, high photo-current responsivity of 6.75 A/W, and high EQE of 1,266%. The standard p–n junction band profile of the heterojunctions is theoretically calculated by the VASP, and it fully supports the properties of our device. This work provide a new type of heterojunction with favorable qualities that can opens up new vistas of research for future electronic and optoelectronic devices. It is worth mentioning that further optimization of the number of atomic layers or stacked sequence of the components could engender new platforms for high-performance and multifunctional devices.

4 Methods

Heterostructure fabrication: We processed vertical stacks of $ReSe_2/MoS_2$ heterostructures with a mechanical transfer technique, a dependable method for fabricating complex systems such as heterostructures. Both $ReSe_2$ and MoS_2 flakes were prepared by using the mechanical exfoliation method. Subsequently, with a spin processor running at 3,000 r/s, we dripped a few drops of the self-regulating polymethyl methacrylate (PMMA) solution on the substrate with $ReSe_2$ flakes. Then, the substrate was placed on the hot plate, heated for 30 min at 150 ℃ and immersed in the NaOH solution at 100 ℃ until the PMMA thin film could be taken off from the substrate. Finally, the film carrying almost all $ReSe_2$ flakes was shifted over the substrate with MoS_2 flakes to make the two chosen nanoflakes combine. We employed acetone as the solubilizer to dissolve the organic PMMA, leaving the inorganic $ReSe_2$ flakes on the substrate. The whole fabrication process was thus accomplished.

(Opto)electronic device fabrication and characterization: Film electrodes contacts with 5-nm-thick Cr and 80-nm-thick Au were fabricated by standard photolithography and e-beam evaporation. The Raman measurements were conducted on a confocal laser Raman spectrometer (Renishaw Model inVia-Reflex) with He–Ne laser (532 nm) excitation. Samples were further characterized by AFM (Benyuan Nano-Instruments Ltd. Model CSPM 5500A) to confirm the number of layers. The FET characterization was performed using Agilent B2902 at room temperature under ambient conditions. The optoelectronic properties were measured on the same electrical measurement system combined with a red laser source (632 nm).

Acknowledgements

This work was supported by the "Hundred Talents Program" of Chinese Academy of Sciences (CAS),

the National Natural Science Foundation of China (No. 91233120), and the CAS/SAFEA International Partnership Program for Creative Research Teams.

Electronic Supplementary Material: Supplementary material (electronic properties of constituent part; Energy dispersive X-ray spectroscopy of the $ReSe_2$ flake; *I*–*T* curve in the case of four representative wavelength sources; properties of $MoS_2/ReSe_2$ heterojunction device; summary of the $ReSe_2/MoS_2$ heterojunction devices) is available in the online version of this article at http://dx.doi.org/10.1007/s12274-015-0932-6.

References

[1] Dean, C.; Young, A. F.; Wang, L.; Meric, I.; Lee, G. H.; Watanabe, K.; Taniguchi, T.; Shepard, K.; Kim, P.; Hone, J. Graphene based heterostructures. *Solid State Commun.* **2012**, *152*, 1275–1282.

[2] Lee, C. H.; Lee, G. H.; van der Zande, A. M.; Chen, W. C.; Li, Y. L.; Han, M. Y.; Cui, X.; Arefe, G.; Nuckolls, C.; Heinz, T. F. et al. Atomically thin p–n junctions with van der waals heterointerfaces. *Nat. Nanotechnol.* **2014**, *9*, 676–681.

[3] Zhang, Y. J.; Dong, H. L.; Tang, Q. X.; Ferdous, S.; Liu, F.; Mannsfeld, S. C. B.; Hu, W. P.; Briseno, A. L. Organic single-crystalline p–n junction nanoribbons. *J. Am. Chem. Soc.* **2010**, *132*, 11580–11584.

[4] Fang, H.; Battaglia, C.; Carraro, C.; Nemsak, S.; Ozdol, B.; Kang, J. S.; Bechtel, H. A.; Desai, S. B.; Kronast, F.; Unal, A. A. et al. Strong interlayer coupling in van der waals heterostructures built from single-layer chalcogenides. *Proc. Natl. Acad. Sci. USA* **2014**, *111*, 6198–6202.

[5] Tongay, S.; Zhou, J.; Ataca, C.; Lo, K.; Matthews, T. S.; Li, J. B.; Grossman, J. C.; Wu, J. Q. Thermally driven crossover from indirect toward direct bandgap in 2D semiconductors: $MoSe_2$ versus MoS_2. *Nano Lett.* **2012**, *12*, 5576–5580.

[6] Zhu, C. F.; Zeng, Z. Y.; Li, H.; Li, F.; Fan, C. H.; Zhang, H. Single-layer MoS_2-based nanoprobes for homogeneous detection of biomolecules. *J. Am. Chem. Soc.* **2013**, *135*, 5998–6001.

[7] Zhou, K.-G.; Zhao, M.; Chang, M.-J.; Wang, Q.; Wu, X.-Z.; Song, Y. L.; Zhang, H.-L. Size-dependent nonlinear optical properties of atomically thin transition metal dichalcogenide nanosheets. *Small* **2015**, *11*, 694–701.

[8] Fan, C.; Li, T.; Wei, Z. M.; Huo, N. J.; Lu, F. Y.; Yang, J. H.; Li, R. X.; Yang, S. X.; Li, B.; Hu, W. P. et al. Novel micro-rings of molybdenum disulfide (MoS_2). *Nanoscale* **2014**, *6*, 14652–14656.

[9] Yang, S. X.; Tongay, S.; Yue, Q.; Li, Y. T.; Li, B.; Lu, F. Y. High-performance few-layer Mo-doped $ReSe_2$ nanosheet photodetectors. *Sci. Rep.* **2014**, *4*, 5442.

[10] Yang, S. X.; Tongay, S.; Li, Y.; Yue, Q.; Xia, J. B.; Li, S. S.; Li, J. B.; Wei, S. H. Layer-dependent electrical and optoelectronic responses of $ReSe_2$ nanosheet transistors. *Nanoscale* **2014**, *6*, 7226–7231.

[11] Yang, S. X.; Wang, C.; Sahin, H.; Chen, H.; Li, Y.; Li, S. S.; Suslu, A.; Peeters, F. M.; Liu, Q.; Li, J. B. et al. Tuning the optical, magnetic, and electrical properties of $ReSe_2$ by nanoscale strain engineering. *Nano Lett.* **2015**, *15*, 1660–1666.

[12] Cui, G. L.; Zhang, M. Z.; Zou, G. T. Resonant tunneling modulation in quasi-2D Cu_2O/SnO_2 p–n horizontal-multi-layer heterostructure for room temperature H_2S sensor application. *Sci. Rep.* **2013**, *3*, 1250.

[13] Mak, K. F.; Lee, C.; Hone, J.; Shan, J.; Heinz, T. F. Atomically thin MoS_2: A new direct-gap semiconductor. *Phys. Rev. Lett.* **2010**, *105*, 136805.

[14] Yu, W. J.; Li, Z.; Zhou, H. L.; Chen, Y.; Wang, Y.; Huang, Y.; Duan, X. F. Vertically stacked multi-heterostructures of layered materials for logic transistors and complementary inverters. *Nat. Mater.* **2013**, *12*, 246–252.

[15] Yu, W. J.; Liu, Y.; Zhou, H. L.; Yin, A. X.; Li, Z.; Huang, Y.; Duan, X. F. Highly efficient gate-tunable photocurrent generation in vertical heterostructures of layered materials. *Nat. Nanotechnol.* **2013**, *8*, 952–958.

[16] Liang, L. B.; Meunier, V. First-principles Raman spectra of MoS_2, WS_2 and their heterostructures. *Nanoscale* **2014**, *6*, 5394–5401.

[17] Radisavljevic, B.; Radenovic, A.; Brivio, J.; Giacometti, V.; Kis, A. Single-layer MoS_2 transistors. *Nat. Nanotechnol.* **2011**, *6*, 147–150.

[18] Wang, Z. X.; Xu, K.; Li, Y. C.; Zhan, X. Y.; Safdar, M.; Wang, Q. S.; Wang, F. M.; He, J. Role of Ga vacancy on a multilayer GaTe phototransistor. *ACS Nano* **2014**, *8*, 4859–4865.

[19] Xu, K.; Wang, Z. X.; Du, X. L.; Safdar, M.; Jiang, C.; He, J. Atomic-layer triangular WSe_2 sheets: Synthesis and layer-dependent photoluminescence property. *Nanotechnology* **2013**, *24*, 465705.

[20] Wang, Z. X.; Safdar, M.; Mirza, M.; Xu, K.; Wang, Q. S.; Huang, Y.; Wang, F. M.; Zhan, X. Y.; He, J. High-performance flexible photodetectors based on GaTe nanosheets. *Nanoscale* **2015**, *7*, 7252–7258.

[21] Haigh, S. J.; Gholinia, A.; Jalil, R.; Romani, S.; Britnell, L.; Elias, D. C.; Novoselov, K. S.; Ponomarenko, L. A.; Geim, A. K.; Gorbachev, R. Cross-sectional imaging of individual layers and buried interfaces of graphene-based heterostructures and superlattices. *Nat. Mater.* **2012**, *11*, 764–767.

[22] Hong, X. P.; Kim, J.; Shi, S. F.; Zhang, Y.; Jin, C. H.; Sun, Y. H.; Tongay, S.; Wu, J. Q.; Zhang, Y. F.; Wang, F. Ultrafast charge transfer in atomically thin MoS_2/WS_2 heterostructures. *Nat. Nanotechnol.* **2014**, *9*, 682–686.

[23] Tongay, S.; Fan, W.; Kang, J.; Park, J.; Koldemir, U.; Suh, J.; Narang, D. S.; Liu, K.; Ji, J.; Li, J. B. et al. Tuning interlayer coupling in large-area heterostructures with CVD-grown MoS_2 and WS_2 monolayers. *Nano Lett.* **2014**, *14*, 3185–3190.

[24] Geim, A. K.; Grigorieva, I. V. Van der waals heterostructures. *Nature* **2013**, *499*, 419–425.

[25] Ho, C. H.; Huang, Y. S.; Chen, J. L.; Dann, T. E.; Tiong, K. K. Electronic structure of ReS_2 and $ReSe_2$ from first-principles calculations, photoelectron spectroscopy, and electrolyte electroreflectance. *Phys. Rev. B* **1999**, *60*, 15766–15771.

[26] Kang, J.; Li, J. B.; Li, S. S.; Xia, J. B.; Wang, L. W. Electronic structural moiré pattern effects on MoS_2/$MoSe_2$ 2D heterostructures. *Nano Lett.* **2013**, *13*, 5485–5490.

[27] Friemelt, K.; Lux-Steiner, M.-Ch.; Bucher, E. Optical properties of the layered transition-metal-dichalcogenide ReS_2: Anisotropy in the van der Waals plane. *J. Appl. Phys.* **1993**, *74*, 5266–5268.

[28] Cheng, R.; Li, D. H.; Zhou, H. L.; Wang, C.; Yin, A. X.; Jiang, S.; Liu, Y.; Chen, Y.; Huang, Y.; Duan, X. F. Electroluminescence and photocurrent generation from atomically sharp WSe_2/MoS_2 heterojunction p–n diodes. *Nano Lett.* **2014**, *14*, 5590–5597.

[29] Lei, S. D.; Sobhani, A.; Wen, F. F.; George, A.; Wang, Q. Z.; Huang, Y. H.; Dong, P.; Li, B.; Najmaei, S.; Bellah, J. et al. Ternary $CuIn_7Se_{11}$: Towards ultra-thin layered photodetectors and photovoltaic devices. *Adv. Mater.* **2014**, *26*, 7666–7672.

[30] Furchi, M. M.; Pospischil, A.; Libisch, F.; Burgdörfer, J.; Mueller, T. Photovoltaic effect in an electrically tunable van der Waals heterojunction. *Nano Lett.* **2014**, *14*, 4785–4791.

[31] Yin, Z. Y.; Li, H.; Li, H.; Jiang, L.; Shi, Y. M.; Sun, Y. H.; Lu, G.; Zhang, Q.; Chen, X. D.; Zhang, H. Single-layer MoS_2 phototransistors. *ACS Nano* **2012**, *6*, 74–80.

[32] Fang, X. S.; Hu, L. F.; Huo, K. F.; Gao, B.; Zhao, L. J.; Liao, M. Y.; Chu, P. K.; Bando, Y.; Golberg, D. New ultraviolet photodetector based on individual Nb_2O_5 nanobelts. *Adv. Funct. Mater.* **2011**, *21*, 3907–3915.

[33] Hu, P. A.; Wen, Z. Z.; Wang, L. F.; Tan, P. H.; Xiao, K. Synthesis of few-layer GaSe nanosheets for high performance photodetectors. *ACS Nano* **2012**, *6*, 5988–5994.

[34] Huo, N. J.; Kang, J.; Wei, Z. M.; Li, S.-S.; Li, J. B.; Wei, S.-H. Novel and enhanced optoelectronic performances of multilayer MoS_2-WS_2 heterostructure transistors. *Adv. Funct. Mater.* **2014**, *24*, 7025–7031.

[35] Tsai, D.-S.; Liu, K.-K.; Lien, D.-H.; Tsai, M.-L.; Kang, C.-F.; Lin, C.-A.; Li, L.-J.; He, J.-H. Few-layer MoS_2 with high broadband photogain and fast optical switching for use in harsh environments. *ACS Nano* **2013**, *7*, 3905–3911.

[36] Huo, N.; Yang, S.; Wei, Z.; Li, S.-S.; Xia, J.-B.; Li, J. Photoresponsive and gas sensing field-effect transistors based on multilayer WS_2 nanoflakes. *Sci. Rep.* **2014**, *4*, 5209.

[37] Hafner, J. *Ab-initio* simulations of materials using VASP: Density-functional theory and beyond. *J. Comput. Chem.* **2008**, *29*, 2044–2078.

[38] Perdew, J. P.; Burke, K.; Ernzerhof, M. Generalized gradient approximation made simple. *Phys. Rev. Lett.* **1996**, *77*, 3865–3868.

[39] Jiang, L. L.; Wu, B.; Liu, H. T.; Huang, Y.; Chen, J. Y.; Geng, D. C.; Gao, H. J.; Liu, Y. Q. A general approach for fast detection of charge carrier type and conductivity difference in nanoscale materials. *Adv. Mater.* **2013**, *25*, 7015–7019.

[40] Doghish, M. Y.; Ho, F. D. A comprehensive analytical model for metal-insulator-semiconductor (MIS) devices: A solar-cell application. *IEEE Trans. Electron Devices* **1993**, *40*, 1446–1454.

[41] Tran, D. P.; Macdonald, T. J.; Wolfrum, B.; Stockmann, R.; Nann, T.; Offenhäusser, A.; Thierry, B. Photoresponsive properties of ultrathin silicon nanowires. *Appl. Phys. Lett.* **2014**, *105*, 231116.

[42] Wang, Q. H.; Kalantar-Zadeh, K.; Kis, A.; Coleman, J. N.; Strano, M. S. Electronics and optoelectronics of two-dimensional transition metal dichalcogenides. *Nat. Nanotechnol.* **2012**, *7*, 699–712.

[43] Wang, Y. J.; Wang, Q. S.; Zhan, X. Y.; Wang, F. M.; Safdar, M.; He, J. Visible light driven type II heterostructures and their enhanced photocatalysis properties: A review. *Nanoscale* **2013**, *5*, 8326–8339.